



A comprehensive characterization of empirical parameterizations for OH exposure in the Aerodyne Potential Aerosol Mass Oxidation Flow Reactor (PAM-OFR)

Qianying Liu^{1,2,3}, Dan Dan Huang³, Andrew T. Lambe⁴, Shengrong Lou³, Lulu Zeng^{1,2}, Yuhang Wu³, Congyan Huang³, Shikang Tao³, Xi Cheng⁵, Qi Chen⁶, Ka In Hoi^{1,2}, Hongli Wang³, Kai Meng Mok^{1,2}, Cheng Huang^{3,7}, and Yong Jie Li^{1,2}

¹Department of Civil and Environmental Engineering, Faculty of Science and Technology, University of Macau, Taipa, Macau SAR, 999078, China

²Department of Ocean Science and Technology, Faculty of Science and Technology, University of Macau, Taipa, Macau SAR, 999078, China

³State Environmental Protection Key Laboratory of Formation and Prevention of Urban Air Pollution Complex, Shanghai Academy of Environmental Sciences, Shanghai, 200233, China

⁴Aerodyne Research Inc., Billerica, Massachusetts, 01821, United States

⁵School of Chemical and Environmental Engineering, China University of Mining and Technology (Beijing), Beijing 100083, China

⁶State Key Joint Laboratory of Environmental Simulation and Pollution Control, BIC-ESAT and IJRC, College of Environmental Sciences and Engineering, Peking University, Beijing, China

⁷Shanghai Environmental Monitoring Center, Shanghai, 200030, China

Correspondence: Dan Dan Huang (huangdd@saes.sh.cn) and Yong Jie Li (yongjieli@um.edu.mo)

Received: 30 August 2024 – Discussion started: 30 September 2024

Revised: 18 February 2025 – Accepted: 20 March 2025 – Published: 12 June 2025

Abstract. The oxidation flow reactor (OFR) has been widely used to simulate secondary organic aerosol (SOA) formation in laboratory and field studies. OH exposure (OH_{exp}), representing the extent of hydroxyl (OH) radical oxidation and normally expressed as the product of OH concentration and residence time in the OFR, is important in assessing the oxidation chemistry in SOA formation. Several models have been developed to quantify the OH_{exp} in OFRs, and empirical equations have been proposed to parameterize OH_{exp} . Practically, the empirical equations and the associated parameters are derived under atmospheric relevant conditions (i.e., external OH reactivity) with limited variations in calibration conditions, such as residence time, water vapor mixing ratio, and ozone (O_3) concentration. Whether the equations or parameters derived under limited sets of calibration conditions can accurately predict the OH_{exp} under dynamically changing experimental conditions with large variations (i.e., extremely high external OH reactivity) in real applications remains uncertain. In this study, we conducted 62 sets

of experiments (416 data points) under a wide range of experimental conditions to evaluate the scope of the application of the empirical equations to estimate OH_{exp} . Sensitivity tests were also conducted to obtain a minimum number of data points, which is necessary for generating the fitting parameters. We showed that, for the OFR185 mode (185 nm lamps with internal O_3 generation), except for external OH reactivity, the parameters obtained within a narrow range of calibration conditions can be extended to estimate the OH_{exp} when the experiments are in wider ranges of conditions. For example, parameters derived within a narrow water vapor mixing ratio range (0.49 %–0.99 %, corresponding to 15.1 %–30.8 % of relative humidity at 101.325 kPa and 298 K) can be extended to estimate the OH_{exp} under the entire range of water vapor mixing ratios (0.49 %–2.76 %, equivalent to 15.1 %–85.7 % of relative humidity under identical conditions). However, the parameters obtained when the external OH reactivity is below 23 s^{-1} could not be used to reproduce the OH_{exp} under the entire range of external OH re-

activity ($4\text{--}204\text{ s}^{-1}$). For the OFR254 mode (254 nm lamps with external O_3 generation), all parameters obtained within a narrow range of conditions can be used to estimate OH_{exp} accurately when experimental conditions are extended. Additionally, when using the OFR254 mode, lamp voltages that are too low should be avoided, as they will generally result in large deviations in the estimations of OH_{exp} from empirical equations. Regardless of whether the OFR185 or OFR254 mode is used, at least 20–30 data points from sulfur dioxide (SO_2) or carbon monoxide (CO) decay with varying conditions are required to fit a set of empirical parameters that can accurately estimate OH_{exp} . Caution should be exercised to use fitted parameters from low external OH reactivity to high ones, for instance, those from direct emissions such as vehicular exhaust and biomass burning.

1 Introduction

As the most important oxidant in tropospheric chemistry (Ehhalt, 1999), the hydroxyl (OH) radical is vital in oxidizing primary pollutants such as volatile organic compounds (VOCs) and contributes to secondary organic aerosol (SOA) and tropospheric ozone (O_3) formation. The OH radical has daytime concentrations of 10^5 to 10^7 molec. cm^{-3} , exhibiting daily (Cao et al., 2020; Tan et al., 2017), seasonal (Friedman and Farmer, 2018), and spatial (Cao et al., 2020; Stone et al., 2012) variations. An average daily OH radical concentration of 1.5×10^6 molec. cm^{-3} is widely used to estimate the photochemical age of an air mass (Mao et al., 2009). Typical VOCs have second-order rate constants of 10^{-15} to 10^{-10} cm^3 molecule $^{-1}$ s^{-1} with OH radicals (Atkinson and Arey, 2003; Atkinson et al., 2006), which can be translated to atmospheric lifetimes of hours to approximately 1 year (Seinfeld and Pandis, 2016). This situation poses challenges in laboratory experiments to directly simulating the OH oxidation of VOCs, which is one of the most important chemical processes in the Earth's atmosphere.

Smog chambers (Cocker et al., 2001; Hildebrandt et al., 2009; Wang et al., 2014) and oxidation flow reactors (OFRs) (George et al., 2007; Kang et al., 2007; Lambe et al., 2011) have been widely employed to simulate the oxidation of VOCs and subsequent SOA formation. For example, the Caltech chamber provides oxidation conditions close to the real atmosphere, making it suitable for the study of complex multi-step reactions and low-volatility products. However, each experiment takes several hours to days, and long-duration experiments are prone to background interference. The Toronto Photo-Oxidation Tube (TPOT) focuses on the study of heterogeneous oxidation reactions of aerosols. Its 0.8 L volume makes it portable, but it is prone to uneven residence time distribution (RTD) and significant wall effects. The Potential Aerosol Mass Oxidation Flow Reactor (PAM-OFR) and the Gothenburg Potential Aerosol Mass Oxidation

Flow Reactor (Go:PAM-OFR) are often used to study the transformation of gaseous precursors into particles (such as the formation of SOA). The Go:PAM-OFR has a volume of 7.2 L, which is only half that of the PAM-OFR, making it suitable for experiments on mobile platforms. However, its small volume gives it the same disadvantages as the TPOT, and it is equipped with only a single ultraviolet (UV) lamp, which does not allow as wide a range of controllable oxidation levels as the PAM-OFR. The PAM's moderate volume and central flow sampling can reduce wall effects.

These OFRs normally operate with high concentrations of oxidants (e.g., OH radicals), which lead to a significant acceleration of oxidation reactions, often by orders of magnitude. To reconcile the differences in OH concentration and exposure time between ambient and laboratory settings, the oxidation extent, i.e., OH exposure (OH_{exp} ; molec. cm^{-3} s), is normally used to extrapolate laboratory findings to ambient conditions. Despite drawbacks such as possible altered reaction mechanisms, this approach provides a quantitative assessment of the chemistry during OH oxidation in a reasonable time span and achievable detection capability. The OH_{exp} has a significant impact on the yield and product distribution during VOC oxidation (Cheng et al., 2021, 2024). Accurate measurement or estimation of the OH_{exp} during laboratory experiments is therefore the key to understanding the oxidation chemistry that can represent the ambient conditions. In this study, we chose to further investigate the PAM-OFR to explore its OH_{exp} , as it offers moderate conditions in terms of experiment time, deployment complexity, range of oxidation levels, and wall effects.

The Aerodyne Potential Aerosol Mass OFR (PAM-OFR) is one of the most widely used OFRs for studying SOA formation and evolution (Zhang et al., 2024). It can achieve a wide range of atmospheric OH_{exp} conditions within short residence times on the order of minutes (Kang et al., 2007; Lambe et al., 2011). The PAM-OFR can be operated in a number of modes, depending on (1) the wavelength of the ultraviolet (UV) light source, (2) the concentration of the externally generated O_3 (if any), and (3) the injection of an external precursor to generate NO_x ($=\text{NO} + \text{NO}_2$) or other oxidants (e.g., nitrate radical or halogen atoms) upon photolysis. The most widely used methods for OH generation include combined photolysis of O_2 and H_2O at $\lambda = 185$ nm plus photolysis of O_3 at $\lambda = 254$ nm (OFR185; Reactions R1–R6) or photolysis of externally added O_3 at $\lambda = 254$ nm (OFR254; Reactions R5–R6) (Rowe et al., 2020):



To obtain the OH_{exp} under these two modes in the PAM-OFR, one can perform decay experiments on trace gases, such as sulfur dioxide (SO_2) and carbon monoxide (CO), and fit the OH_{exp} based on known second-order rate constants between the OH radical and the trace gases, defined as $\text{OH}_{\text{exp, dec}}$. Based on the results of the decay experiments, Li et al. (2015) and Peng et al. (2015) developed estimation equations to parameterize OH_{exp} as a function of easily measurable quantities, which is denoted as $\text{OH}_{\text{exp, est}}$. A set of parameters (a – f and x – z , respectively) for the estimation equations of the OFR185 and OFR254 modes (see Sect. 2.3 for details) was obtained by fitting the estimation equations to $\text{OH}_{\text{exp, dec}}$ values obtained from decay experiments.

When using the PAM-OFR in field studies, it is necessary to obtain concurrent OH_{exp} that is representative of the ambient conditions. However, environmental conditions in field studies (e.g., humidity, temperature) are constantly changing, making it challenging to replicate these conditions for OH_{exp} estimation. In some field studies using the PAM-OFR, concurrent OH_{exp} was estimated by measuring the relative decay of benzene and toluene (Liao et al., 2021; Liu et al., 2018). Additionally, some studies have mentioned that OH concentrations can be indirectly measured by detecting the decay of tracers such as 3-pentanol, 3-pentanone, pinonaldehyde, or butanol- d_9 (Barnet et al., 2012). However, the measurement of all these organic tracers requires specific, sophisticated instruments such as proton-transfer-reaction time-of-flight mass spectrometers (PTR-TOF-MSs). Additionally, switching the instrument back and forth between the front and end of the OFR during field measurements can result in some loss of real-time VOC data before entering the OFR. To obtain accurate OH_{exp} , some studies explicitly modeled the radical chemistry in the PAM-OFR (Li et al., 2015; Ono et al., 2014; Peng et al., 2015). The estimation equations developed by Li et al. (2015) and Peng et al. (2015), although empirical, reproduced the OH_{exp} from models within 10 %, making them a good choice because these equations only require the input of a few easily available parameters. However, it is unclear whether the fitted parameters obtained under certain conditions can still accurately estimate OH_{exp} when experimental conditions, such as UV light intensity, water vapor mixing ratio, residence time, and external OH reactivity (OHR_{ext}), undergo significant changes. Furthermore, there is currently no consensus on the minimum number of decay experiments required to obtain accurate parameterization for OH_{exp} estimation using these equations. This facet is important for field studies using the PAM-OFR where only limited numbers of decay experiments can be performed to obtain concurrent OH_{exp} estimation.

In this study, we conduct a series of experiments using the decay of SO_2 and CO to estimate the OH_{exp} in the PAM-OFR under the OFR185 and OFR254 modes. The applicability of previously developed OH_{exp} estimation equations to obtain accurate OH_{exp} in the PAM-OFR is evaluated by linear regression of $\text{OH}_{\text{exp, est}}$ against $\text{OH}_{\text{exp, dec}}$. We also evaluate

how well estimation equations perform when using limited ranges of experimental parameters (e.g., OHR_{ext} , residence time, water mixing ratio) or different trace gases (SO_2 and CO) and provide recommendations. In addition, we propose the minimal number of trace gas decay experiments required to obtain a set of usable parameters for the OH_{exp} estimation equations. Finally, we also compare the advantages and disadvantages of the OFR185 and the OFR254 modes from the perspective of the quantification of OH_{exp} . The methodology of this study can be applied to laboratory and field experiments for OH_{exp} estimation using the PAM-OFR or other OFRs that follow a plug flow assumption.

2 Methods

2.1 The PAM-OFR

Experiments were conducted using an Aerodyne PAM-OFR (Aerodyne Research Inc., Billerica, MA, US), which is a horizontal aluminum cylindrical chamber with an internal volume of 13.3 L. The PAM-OFR operates in continuous-flow mode. Four low-pressure Hg lamps are installed inside the reactor to produce UV light with characteristic spectral lines (e.g., 185 and 254 nm). The OH is generated via OFR185 using two ozone-producing Hg lamps (GPH436T5VH/4P, Light Sources, Inc.) or via OFR254 using two ozone-free Hg lamps (GPH436T5L/4P, Light Sources, Inc.) to photolyze externally added ozone. A flow of nitrogen purge gas, ranging from 0.2 to 0.3 L min^{-1} , is introduced between the lamps and sleeves. This nitrogen gas flow serves to reduce the heat generated by the lamps and prevent the formation and accumulation of ozone between the lamps and the quartz tubes that isolate them from the sample flow in the OFR. A fluorescent dimming ballast is used to control the photon flux by regulating the voltage applied to the lamps, which allows us to generate different OH concentrations. In typical measurement sequences, nine lamp voltage settings (including lights off) were cycled through every 2–3 h. The dimming voltage ranged from 0 to 10 V direct current (DC).

2.2 OH_{exp} estimation through decay of SO_2 and CO ($\text{OH}_{\text{exp, dec}}$)

OH_{exp} can be indirectly measured by detecting the decay of the tracers with known reaction rates. Inorganic trace gases (SO_2 or CO) react with OH radicals at slower rates compared to most VOCs. However, considering the complex oxidation chemistry of VOCs, SO_2 and CO can better capture the features of real OHR_{ext} decay and effective OHR_{ext} (Peng et al., 2015). We performed systematic decay experiments with SO_2 and CO in the PAM-OFR, with conditions tabulated in Tables S1 and S2 in the Supplement. Figure S1 shows the schematics of the experimental setups in the OFR185 and OFR254 modes. In the OFR185 mode, the injected gas flow at the inlet of the PAM is made up of three sub-flows:

(1) the trace gas flow, i.e., SO₂ of 0.2–8.7 ppm or CO of 10.2–207.5 ppm supplied from gas cylinders (purity: 99.9 % of SO₂, 99.95 % of CO; Shanghai Shenkai Gases Technology CO., LTD.); (2) dry clean air from a zero-air generator (ZAS-100/150, Convenient) with a non-methane hydrocarbon content of less than 1 ppb; and (3) the humidified clean air passed through a Nafion humidifier (FC100-80-6MSS, Perma Pure). By adjusting the ratio of dry air to humidified air, the water vapor mixing ratio in the PAM-OFR can be controlled. Additionally, they also serve as makeup flows to maintain a constant flow rate. At the outlet of the reactor, the gas flow was sampled from an internal perforated Teflon ring. The gas-phase species (O₃, SO₂, and CO) were detected using an ultraviolet ozone analyzer (UV-100, Eco Sensors), an SO₂ monitor (Model 43i, Thermo Scientific), and a CO monitor (G2401, Picarro), respectively. In the OFR254 mode, in addition to the previously mentioned setup, externally generated O₃ (through UV photolysis) with desired concentrations was injected at the inlet of the PAM-OFR.

Figure S2a and b depict examples of set and measured parameters during experiments conducted in the OFR185 and OFR254 modes, respectively. In the OFR185 mode, without radical generation to oxidize the tracer species, their concentration was allowed to stabilize under dark conditions. Once the concentration reached a steady state, the UV lamps were turned on. Different light intensities lead to varying levels of decay of SO₂ or CO after oxidation, reflecting different OH_{exp} within the PAM-OFR. In the OFR254 mode, it is necessary to obtain the initial concentration of O₃ injected into the PAM-OFR in the absence of OHR_{ext}. While the SO₂ or CO concentration was in the process of stabilizing, the O₃ flow was temporarily blocked outside the PAM-OFR using a valve. Dry clean air was then introduced to compensate for this portion of the flow, ensuring a constant total flow throughout the entire process. Once the tracer species concentration had reached a steady state, the O₃ was then allowed to flow into the PAM-OFR. The total OH_{exp, dec} in the reactor was varied over a wide range (approximately 10⁹–10¹² molec. cm⁻³ s) by changing the UV light intensity, water mixing ratio, and residence time. The mean residence time was obtained from the ratio of the internal volume of and the total flow rate through the PAM-OFR. In the calculation of OH_{exp, dec} (see the paragraph below), plug flow conditions were assumed, and this has been shown by Li et al. (2015) and Peng et al. (2015) to agree with the RTD approach for OH_{exp} when using species (such as SO₂ or CO) with low reaction rate constants with OH radicals (*k_{i, OH}*).

OH_{exp, dec} in the PAM-OFR was calculated from the pseudo-first-order reaction of OH with SO₂ or CO, whose *k_{i, OH}* values have been well characterized (*k_{SO₂, OH}* = 9.49 × 10⁻¹³ cm³ molec.⁻¹ s⁻¹ and *k_{CO, OH}* = 2.4 × 10⁻¹³ cm³ molec.⁻¹ s⁻¹ at 1 atm and 298 K) (Burkholder et al., 2020; Cao et al., 2020). By measuring the decay of SO₂ or CO, the corresponding OH_{exp, dec} is

calculated as follows:

$$\text{OH}_{\text{exp, dec}} = \frac{-1}{k_{i, \text{OH}}} \times \ln \left(\frac{C_{i, \text{out}}}{C_{i, \text{in}}} \right), \quad (1)$$

where *C_{i, in}* is the concentration of reactant *i* injected into the PAM-OFR (ppb), *C_{i, out}* is the reactant *i* concentration at the PAM-OFR outlet (ppb), and *k_{i, OH}* is the second-order rate constant between the trace species (SO₂ or CO) and OH radicals.

Despite the use of nitrogen as a purge gas to reduce the heat generated by the lamp, temperature variations were still observed within the PAM-OFR. There was a maximum deviation of approximately 13 °C from 25 °C when using SO₂ as the OHR source. However, the *k_{SO₂, OH}* was 8.85 × 10⁻¹³ cm³ molec.⁻¹ s⁻¹ at 38 °C (Burkholder et al., 2020), which results in the calculated OH_{exp, dec} being only approximately 7 % higher than that derived from *k_{SO₂, OH}* at 25 °C. Pan et al. (2024) noted that temperature increases caused by lamp heating exerted minimal influence on gas-phase reaction rates, with SO₂ decay and OH exposure showing negligible variations. Therefore, the influence of temperature on reaction kinetics was not considered in this study.

2.3 OH_{exp} estimation from empirical equations (OH_{exp, est})

Li et al. (2015) proposed an OH_{exp, est} estimation equation (Eq. 2) for OFR185 based on easily measurable quantities:

$$\text{OH}_{\text{exp, est}} = 10^{\left[a + \left(b + c \times \text{OHR}_{\text{ext}}^d + e \times \log \left(\text{O}_{3, \text{out}} \times \frac{180}{t} \right) \times \text{OHR}_{\text{ext}}^f \right) \times \log \left(\text{O}_{3, \text{out}} \times \frac{180}{t} \right) + \log \text{H}_2\text{O} + \log \left(\frac{t}{180} \right) \right]}, \quad (2)$$

where *a*–*f* are fitting parameters (values are reported in Table S5); O_{3, out} is the ozone concentration measured at the exit of the PAM-OFR (molec. cm⁻³), which serves as a surrogate for UV flux; H₂O is the water vapor mixing ratio in the PAM-OFR (%), which is influenced by both temperature and relative humidity; and *t* is mean residence time (s). The total external OH reactivity is represented by OHR_{ext} (s⁻¹) = ∑_{*i*} *k_i* [*C_i*], where *k_i* and [*C_i*] are the rate constants with OH and the concentration of the OH-consuming reactant *i* in the system (Wang et al., 2020).

Peng et al. (2015) proposed another equation (Eq. 3) for OH_{exp, est} in OFR254:

$$\text{OH}_{\text{exp, est}} = 10^{\left[x + \log(-\log r_{\text{O}_3}) + y \times \left(\frac{\text{OHR}_{\text{ext}}}{\text{O}_{3, \text{in}}} \right)^z \right]}, \quad (3)$$

where *x*–*z* are fitting parameters (values are reported in Table S6); log *r_{O₃}* (log(O_{3, out}/O_{3, in})) is the logarithm of the ratio between the output and input O₃ concentrations, which serves as a surrogate for UV flux and also captures the effect of H₂O; and O_{3, in} is the concentration of externally injected O₃ into the PAM-OFR (molecules cm⁻³).

In total, we performed 62 sets of trace gas decay experiments with 416 data points for the $\text{OH}_{\text{exp, dec}}$, with 25 sets and 175 data points in the OFR185 mode and 37 sets and 241 data points in the OFR254 mode. In the OFR185 mode, the 175 experiments cover an $\text{OH}_{\text{exp, dec}}$ range of 3.57×10^8 – 5.52×10^{12} molec. cm^{-3} s, with an equivalent photochemical age ranging from 4 min to 43 d. In the OFR254 mode, the 241 experiments cover an $\text{OH}_{\text{exp, dec}}$ range of 1.01×10^9 – 2.18×10^{12} molec. cm^{-3} s, with an equivalent photochemical age ranging from 11 min to 17 d. The error in $\text{OH}_{\text{exp, dec}}$ is derived from the measurement error of the tracer gas, propagated through Eq. (1). When $\text{OH}_{\text{exp, dec}}$ ranged from 3.6×10^8 – 5.5×10^{12} molec. cm^{-3} s, the resulting error values were 1.9×10^8 – 2.4×10^{10} molec. cm^{-3} s.

After obtaining the $\text{OH}_{\text{exp, dec}}$ values, we used Eqs. (2) and (3) to fit the parameters a – f and x – z for the OFR185 and OFR254 modes, respectively, given that the experimental parameters, such as OHR_{ext} , $\text{O}_{3, \text{out}}$, H_2O , and t (in Eq. 2) as well as r_{O_3} , OHR_{ext} , and $\text{O}_{3, \text{in}}$ (in Eq. 3), are known. The $\text{OH}_{\text{exp, est}}$ values were then reconstructed with the fitted parameters and the experimental parameters and were compared with the $\text{OH}_{\text{exp, dec}}$ values via linear regression analysis. Similarly, the error values for all $\text{OH}_{\text{exp, est}}$ values are at least 1 order of magnitude smaller than the respective $\text{OH}_{\text{exp, est}}$ values. The generation of OH radicals in the PAM-OFR is related to the photon fluxes at $\lambda = 185$ nm (I_{185}) and $\lambda = 254$ nm (I_{254}). According to Rowe et al. (2020), $I_{185} : I_{254}$ is specific to the Hg lamp utilized. Since the OH_{exp} estimation equation for OFR185 uses O_3 concentration as a measurable surrogate for the UV flux at 185 nm, it is also lamp-specific. Because the UV lamps used in our study are different from the BHK lamps employed by Li et al. (2015), we anticipate that the parameters a – f fitted from our decay experiments (Table S5) should be quite different from those in Li et al. (2015), which is indeed the case. Similarly, fitting parameters x – z for the OFR254 mode from our decay experiments (Table S6) are also different from those in Peng et al. (2015).

3 Results and discussion

3.1 The OFR185 mode: OHR_{ext} level relevant to ambient conditions

Field studies showed that the environmental OHR_{ext} mainly fluctuated between 10–30 s^{-1} (Fuchs et al., 2017; Lou et al., 2010; Lu et al., 2010; Tan et al., 2018; Yang et al., 2017). To investigate the factors that potentially affect the fitting parameters of Eq. (2) in the estimation of OH_{exp} under ambient conditions, we first performed 16 sets of experiments with OHR_{ext} of 4–23 s^{-1} using SO_2 as the OHR_{ext} source. With the measured $\text{OH}_{\text{exp, dec}}$, the parameters (a – f) were first derived, which were used to reconstruct $\text{OH}_{\text{exp, est}}$ using Eq. (2) with known OHR_{ext} , ozone concentration ($\text{O}_{3, \text{out}}$), water va-

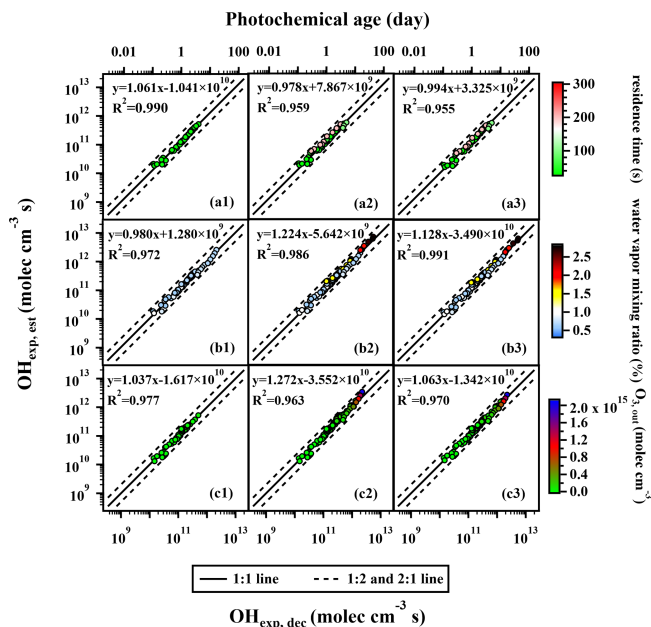


Figure 1. The regression results of $\text{OH}_{\text{exp, est}}$ and $\text{OH}_{\text{exp, dec}}$ when variations occurred in the (a1–a3) residence time, (b1–b3) water vapor mixing ratio, and (c1–c3) output O_3 concentration under atmospheric relevant OHR_{ext} levels (4–23 s^{-1}). Compared to panels (a1), (b1), and (c1), panels (a2), (b2), and (c2) incorporated additional data points with higher t , H_2O , and $\text{O}_{3, \text{out}}$ values, respectively, but still utilized the fitting parameters $\text{FP}_{\text{st}, 185}$, $\text{FP}_{\text{H}_2\text{O}, 185}$, and $\text{FP}_{\text{O}_3, 185}$ obtained from the lower condition range to estimate $\text{OH}_{\text{exp, est}}$. In panels (a3), (b3), and (c3), all data points within the extended condition range were used to refit the parameters a – f , and the resulting $\text{FP}_{\text{et}, 185}$, $\text{FP}_{\text{eH}_2\text{O}, 185}$, and $\text{FP}_{\text{eO}_3, 185}$ were employed to estimate $\text{OH}_{\text{exp, est}}$ (s: short; l: low; e: extended). All the error values for $\text{OH}_{\text{exp, dec}}$ are 0.5 or even 2 orders of magnitude smaller than the corresponding $\text{OH}_{\text{exp, dec}}$ values. When applying a logarithmic scale, the error bars become difficult to represent. To enhance the readability of the graph, error bars are not included. For the same reason, error bars for $\text{OH}_{\text{exp, est}}$ values are also not displayed.

por mixing ratio (H_2O), and residence time (t). The reconstructed $\text{OH}_{\text{exp, est}}$ values were plotted against the $\text{OH}_{\text{exp, dec}}$ values calculated from the trace gas decay experiments, as shown in Fig. 1. The 1 : 2 and 2 : 1 lines indicate a difference of approximately 0.5 orders of magnitude between $\text{OH}_{\text{exp, dec}}$ and $\text{OH}_{\text{exp, est}}$, which is considered to be acceptable as an uncertainty in OH_{exp} estimation.

Firstly, we investigated the effect of changing residence time on the OH_{exp} estimation. With other experimental parameters (i.e., H_2O , $\text{O}_{3, \text{out}}$, and OHR_{ext}) being similar, we set the residence time to a low value (33 s) and also a range of higher values (61–200 s). The detailed ranges of each experimental condition for different datasets are listed in Table S3. With the residence time of 33 s, the reconstructed $\text{OH}_{\text{exp, est}}$ correlates well with the experimental $\text{OH}_{\text{exp, dec}}$ (slope = 1.061 and $R^2 = 0.990$; Fig. 1a1). The set of fit-

ted parameters $a-f$ ($FP_{st,185}$; st : short time) applied in Fig. 1a1 is presented in Table S5. When the residence time was increased to 61–200 s, the interpolated $OH_{exp,est}$ utilizing $FP_{st,185}$ was also in good correlation with $OH_{exp,dec}$ (slope = 0.978, $R^2 = 0.959$; Fig. 1a2). We also derived fitted parameters ($FP_{et,185}$; et : extended t) using the data points with the extended range of residence time (33–200 s). Not surprisingly, with the application of $FP_{et,185}$, $OH_{exp,est}$ also correlated well with $OH_{exp,dec}$ (slope = 0.994, $R^2 = 0.955$; Fig. 1a3). The results indicate that variation in residence time does not significantly affect the fitting parameters of Eq. (2) for the OH_{exp} estimation. From an experimental perspective, since OH_{exp} is the product of OH radical concentration ($[OH]$) and the residence time (t), as long as the change in t does not significantly alter the quasi-steady-state $[OH]$, the fitted parameters from a narrow range of t should be applicable to situations of longer t . Mathematically, two terms of $180/t$ and $t/180$ are related to t , ranging from 0.90–5.45 and 0.18–1.11, respectively, which do not contribute significantly to the exponent in Eq. (2) after taking the logarithm of them. It is important to note that the above discussion regarding residence time assumes plug flow conditions within the PAM-OFR, which are applicable to substances with low $k_{i,OH}$, such as SO_2 (or CO). For species that react rapidly with OH, such as monoterpenes or toluene, localized concentration gradients can develop within the OFR, leading to a significant uneven actual RTD that affects the estimation of OH_{exp} (Palm et al., 2018).

Similarly, we then investigated the impacts of H_2O on the estimation of OH_{exp} . Applying fitted parameters from experiments of low water vapor mixing ratios (0.49%–0.99%; Fig. 1b1) ($FP_{IH_2O,185}$; IH_2O : low H_2O) to data spanning a wide range of water vapor mixing ratios (0.49%–2.76%) also yielded a reasonably good correlation between $OH_{exp,est}$ and $OH_{exp,dec}$ (Fig. 1b2). This could be attributed to the fact that the term $\log H_2O$ in Eq. (2) does not contribute significantly to the exponent.

As for ozone concentration, applying fitting parameters ($FP_{IO_3,185}$; IO_3 : low $O_{3,out}$) from experiments of low ozone concentration (1.44×10^{12} – 6.79×10^{13} molec. cm^{-3} , Fig. 1c1) to reconstruct the data for a wide range (1.44×10^{12} – 2.03×10^{15} molec. cm^{-3}) yielded a reasonably good correlation between $OH_{exp,est}$ and $OH_{exp,dec}$ (Fig. 1c2). It only resulted in a mildly increased slope (from 1.063 to 1.272) and similar R^2 values (both are 0.970) as compared to those using the whole ozone concentration range (Fig. 1c3).

Ideally, trace gas decay experiments covering the entire ranges of the t , H_2O , and $O_{3,out}$ variations under real experimental conditions should be conducted, which is labor-intensive. Practically, due to the atmospherically relevant variations that occur in t , H_2O , and $O_{3,out}$ during the real experiments, the ranges of t , H_2O , and $O_{3,out}$ covered by trace gas decay experiments are usually narrower compared to the real experiments. Our results suggest that the fitting param-

eters ($a-f$) obtained from calibration experiments with relatively narrow ranges of t , H_2O , and $O_{3,out}$ can still provide a reliable estimation of OH radical levels during the real experiments, which would cover wider ranges of these conditions.

It is noteworthy that reliable estimations can be achieved regardless of whether the narrow range is situated within the lower or higher interval of the full condition range. Figure 1 demonstrated the case where the narrow range was situated within the lower interval, while Fig. S3 presented the case where the narrow range was situated within the higher interval. The detailed ranges of each experimental condition for different datasets are listed in Table S3. As shown in Fig. S3, the data points in Fig. S3a1 had residence times of 100–296 s, the data points in Fig. S3b1 had water vapor mixing ratios of 1.04%–2.76%, and the data points in Fig. S3c1 had $O_{3,out}$ of 8.45×10^{13} – 2.03×10^{15} molec. cm^{-3} . Figure S3a2, b2, and c2 built on Fig. S3a1, b1, and c1 by incorporating data points with shorter t (33–61 s), lower H_2O (0.49%–0.97%), and lower $O_{3,out}$ (1.44×10^{12} – 6.79×10^{13} molec. cm^{-3}), respectively, but still used fitting parameters $a-f$ obtained from the higher range of conditions to estimate $OH_{exp,est}$. In Fig. S31a3, b3, and c3, the parameters $a-f$ were refitted using all the data points included in the expanded t , H_2O , and $O_{3,out}$ ranges, respectively, and the obtained $a-f$ were used to estimate $OH_{exp,est}$. Using Fig. S3a1–a3 as an example, the slope and R^2 values in Fig. S3a2 and a3 were very close to 1, reflecting the good consistency between $OH_{exp,est}$ and $OH_{exp,dec}$. In the OFR254 mode discussed later (Fig. 4c1–c3), this narrower range can also be situated within the middle interval of the full condition range. This applicability of fitting parameters obtained from narrow ranges of experimental conditions is beneficial for quickly obtaining concurrent OH_{exp} during the experiments in field measurements.

3.2 The OFR185 mode: OHR_{ext} level relevant to emission sources

The experimental conditions in the PAM-OFR often involve not only general atmospheric conditions ($OHR_{ext} < 30 s^{-1}$) but also high-concentration conditions, e.g., those directly from emission sources. For instance, the OHR_{ext} of direct vehicle emission can be as high as $1000 s^{-1}$, with plenty of reducing gases such as CO and VOCs (Nakashima et al., 2010). To evaluate the applicability of Eq. (2) under situations of high OHR_{ext} , we performed high OHR_{ext} (up to $204 s^{-1}$) experiments using high concentrations of SO_2 as the OHR_{ext} source. Compared to the data points shown in Fig. 2a (4–23 s^{-1}), Fig. 2b and c included additional data points with higher OHR_{ext} values (198–204 s^{-1}), while the other conditions remained similar. In Fig. 2b, the parameters $a-f$ ($FP_{IOHR,185}$; $IOHR$: low OHR_{ext}) obtained from the low OHR_{ext} data points were used to estimate $OH_{exp,est}$, yet those used in Fig. 2c were refitted from the data points with extended OHR_{ext} range (4–204 s^{-1}). It could be observed from Fig. 2b that, when estimating OH_{exp} using $FP_{IOHR,185}$,

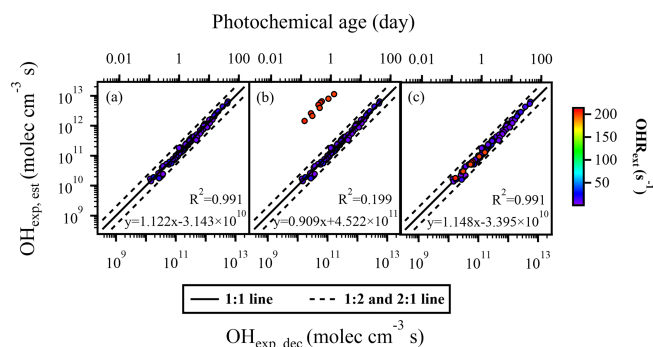


Figure 2. The regression results of $\text{OH}_{\text{exp,est}}$ and $\text{OH}_{\text{exp,dec}}$ with different OHR_{ext} levels. In panel (a), data points with atmospheric relevant OHR_{ext} levels ($4\text{--}22\text{ s}^{-1}$) were applied. In addition to the data points contained within panel (a), panel (b) included additional data points with OHR_{ext} levels related to emission sources ($198\text{--}204\text{ s}^{-1}$), but $\text{FP}_{\text{IOHR},185}$ values were still used to estimate $\text{OH}_{\text{exp,est}}$. In panel (b), data points in red show that the $\text{OH}_{\text{exp,est}}$ values of these high OHR_{ext} data points were significantly overestimated. $\text{FP}_{\text{IOHR},185}$ values were not applicable to high OHR_{ext} conditions. The data points in panel (c) were identical to those in panel (b), but the estimation of $\text{OH}_{\text{exp,est}}$ utilized the $\text{FP}_{\text{eOHR},185}$ obtained by fitting all data points across the full range of OHR_{ext} levels.

$\text{OH}_{\text{exp,est}}$ values of the high OHR_{ext} data points were significantly overestimated, with a difference of more than 2 orders of magnitude compared to $\text{OH}_{\text{exp,dec}}$. This observation suggests that, differently to cases for the residence time, water vapor mixing ratio, and ozone concentration shown in the section above, $\text{FP}_{\text{IOHR},185}$ values were not applicable to high OHR_{ext} conditions.

We then investigated the possible causes of the discrepancy for OH_{exp} estimation between $\text{FP}_{\text{IOHR},185}$ and $\text{FP}_{\text{eOHR},185}$ (eOHR : extended OHR_{ext}). From a mathematical perspective, according to Eq. (2), the third term $c \times \text{OHR}_{\text{ext}}^d \times \log(\text{O}_{3,\text{out}} \times 180/t)$ and the fourth term $e \times \text{OHR}_{\text{ext}}^f \times [\log(\text{O}_{3,\text{out}} \times 180/t)]^2$ are associated with OHR_{ext} and involve fitted parameters of $c\text{--}f$. To investigate their relationships with OHR_{ext} , we performed a sensitivity test with a fixed ozone concentration ($1.77 \times 10^{14}\text{ molec. cm}^{-3}$) and residence time (89 s), which were mean values during our experiments. When using the $c\text{--}f$ values of $\text{FP}_{\text{IOHR},185}$ (-0.13922 , 0.26786 , 0.0026332 , and 0.4917), the variations in the third term, the fourth term, and their sum with respect to OHR_{ext} are shown in Fig. S4a1–a3, respectively. The third term (Fig. S4a1) was negative and decreased as OHR_{ext} increased, while the fourth term (Fig. S4a2) was positive and increased as OHR_{ext} increased. The sum of them (Fig. S4a3), however, firstly decreased and then started to increase at approximately $\text{OHR}_{\text{ext}} = 21\text{ s}^{-1}$, possibly owing to a slower decrease in the third term or a faster increase in the fourth. If contributions from other terms in Eq. (2) were constant, this led to an increase in OH_{exp}

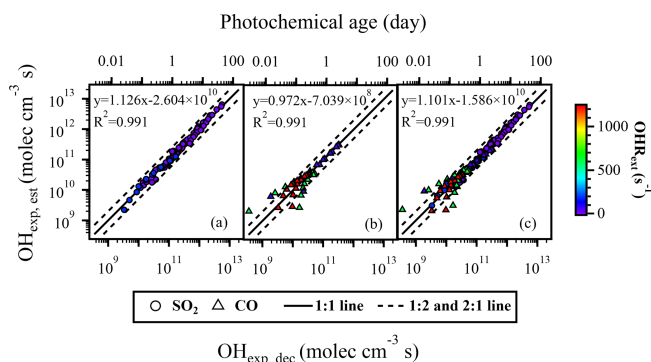


Figure 3. The regression results of $\text{OH}_{\text{exp,dec}}$ and $\text{OH}_{\text{exp,est}}$ in the OFR185 mode with (a) SO_2 and (b) CO as OHR_{ext} sources. (c) Results from all experiments (using SO_2 and CO) in the OFR185 mode.

as OHR_{ext} increased beyond 21 s^{-1} . Our results showed that the expectation that OH_{exp} should decrease with increasing OHR_{ext} (Li et al., 2015) was applicable to the lower ranges of OHR_{ext} , i.e., under atmospheric relevant conditions. With a further increase in OHR_{ext} , i.e., above atmospheric condition, the fitted parameters obtained from the dataset with $\text{FP}_{\text{IOHR},185}$ were not applicable.

When using the $c\text{--}f$ values of $\text{FP}_{\text{eOHR},185}$ (-0.079114 , 0.36805 , 0.0041654 , and 0.38722), the trends of the third and the fourth terms (Fig. S4b1 and b2, respectively) were similar to those with low OHR_{ext} (Fig. S4a1 and a2, respectively); their sum, however, gave a monotonically decreasing trend as OHR_{ext} increased (Fig. S4b3), consistent with the expectation that OH_{exp} should decrease with increasing OHR_{ext} (Li et al., 2015). The curve in Fig. S4b3 can continue to decrease monotonically at higher OHR_{ext} values, at least until 2000 s^{-1} .

From the perspective of oxidation chemistry, high concentrations of gas-phase SO_2 could lead to more SO_2 entering the particle phase. The H_2O_2 in the liquid water of nucleated sulfuric acid aerosols would further oxidize SO_2 (Liu et al., 2020), which could lead to the discrepancy for OH estimation between low OHR and extended high OHR.

Nevertheless, the good agreement between $\text{OH}_{\text{exp,est}}$ and $\text{OH}_{\text{exp,dec}}$ in Fig. 2c (using refitted parameters from the dataset of extended OHR_{ext}) indicates that Eq. (2) can still be used to estimate OH_{exp} under high OHR_{ext} conditions. This conclusion is further supported by the results of OH_{exp} obtained using CO as the OHR_{ext} source (see Fig. 3 and the subsection below) under extremely high OHR_{ext} conditions (up to 1200 s^{-1}). This is advantageous for the use of the PAM-OFR in simulations of SOA formation from direct emission sources (e.g., vehicular exhaust and biomass burning) where OHR_{ext} is extremely high. It is, however, desirable to have OH_{exp} estimated under similarly high OHR_{ext} for those experiments to accurately represent the extent of oxidation.

3.3 The OFR185 mode: SO₂ and CO as OHR_{ext} sources

Peng et al. (2015) suggested that SO₂ can better capture the features of real OHR_{ext} decay and effective OHR_{ext}. The reaction between SO₂ and OH is relatively straightforward and is not expected to undergo too many side reactions. CO is a typical gaseous inorganic compound emitted during combustion process. Using CO as an OHR_{ext} source to explore the estimation of OH_{exp} in the simulation of oxidation chemistry for emission sources (i.e., high OHR_{ext} level) is representative. Therefore, we compared the results with SO₂ (Fig. 3a) and CO (Fig. 3b) as the OHR_{ext} source. When using SO₂ as the OHR_{ext} source, all data points agreed within a factor of 2 (Fig. 3a), while only approximately 83 % of the data points agreed within a factor of 2 when CO was used as the OHR_{ext} source (Fig. 3b). The deviating data points were mostly concentrated in areas with high OHR_{ext} (> 600 s⁻¹) and low O_{3,out} concentration (10¹²–10¹³ molec. cm⁻³), where the removal of CO was relatively low. Li et al. (2015) observed increased deviations between OH_{exp,est} and OH_{exp,dec}, which were attributed, at least in part, to the increased measurement uncertainties for CO when the decrease in its concentration was marginal. We believe that measurement uncertainty might not be the main reason in our case because most of the decreases in CO concentration during our experiments were larger than the precision of the Picarro G2401 Analyzer (~ 1.5 ppb at 5 min time resolution). Another possible reason is that, in addition to the reaction with OH radicals, CO may react with some other oxidants, leading to its consumption, while SO₂ was less affected, thereby resulting in more scattered data points for CO. The reaction rate of CO with HO₂ is very slow and is unlikely to play a significant role ($k_{\text{CO},\text{HO}_2} = 5.55 \times 10^{-27} \text{ cm}^3 \text{ molec.}^{-1} \text{ s}^{-1}$ at 300 K) (You et al., 2007). Cohen and Heicklen (1972) suggested that CO could also react with atomic oxygen (O(¹D)). Clerc and Barat (1967) reported some appreciable rate coefficients (10⁻¹¹ to 10⁻¹² cm³ molec.⁻¹ s⁻¹) for the reaction between CO and O(¹D), which are higher than those for the reactions of CO with OH ($k_{\text{CO},\text{OH}} = 2.4 \times 10^{-13} \text{ cm}^3 \text{ molec.}^{-1} \text{ s}^{-1}$ at 298 K) (Burkholder et al., 2020). It is therefore possible that reaction between CO and O(¹D) might have complicated the decay of CO in the PAM-OFR. To further investigate this aspect, we used the KinSim, a kinetic simulator, to calculate the average mixing ratios of OH, O(¹D), and HO₂ under the specific conditions in the PAM-OFR and then assessed the relative importance of the reactions CO + OH → CO₂ + H, CO + O(¹D) → CO₂, and CO + HO₂ → CO₂ + OH (Li et al., 2015; Peng and Jimenez, 2019, 2020). The results show that, although the reaction rate constant of CO and O(¹D) is 1–2 orders of magnitude higher than that of CO and OH, the concentration of OH is about 6–7 orders of magnitude higher than the concentration of O(¹D), indicating that the reaction of CO with O(¹D) will not have a significant impact on the consumption of CO. The real reason for the scattered data

points when using CO in the trace gas decay experiment is still unknown.

Figure 3c includes the results of trace gas decay experiments using both SO₂ and CO as the OHR_{ext} source. Despite having different reaction rates with OH radicals, the data points could be collectively utilized to fit the parameters for the estimation equation. With approximately 95 % of the results agreeing within a factor of 2, OH_{exp,est} obtained using the fitted parameters exhibited good agreements (slope = 1.101, $R^2 = 0.991$) with OH_{exp,dec}. Our results thus suggest that, although using CO as the OHR_{ext} might result in some scattered data points, it was still feasible to use Eq. (2) to estimate OH_{exp} given that experiments were not performed solely in conditions with high OHR_{ext} (i.e., high CO concentrations) and low O₃ concentrations. Another benefit of using CO as the OHR_{ext} source for the estimation of OH_{exp} is that it introduces complexity in the precursor, which resembled that in real applications. Although not tested in this study, we also note that further trace gas decay experiments in the presence of N₂O / NO_x (typical urban environment) should be conducted when oxidation chemistry in the presence of NO_x is studied (Cheng et al., 2021).

3.4 The OFR254 mode

The equation for OH_{exp} estimation in the OFR254 mode is simpler compared to that of the OFR185 mode. According to Eq. (3), under the OFR254 mode, the three parameters potentially affecting the OH_{exp} are OHR_{ext}, input O₃ concentration, and r_{O_3} . The detailed ranges of each experimental condition for different datasets are listed in Table S4. We found that, compared to Fig. 1, the data points in Fig. 4 were more scattered. Most of the R^2 values in Fig. 4 were below 0.9, indicating that, when using SO₂ as the OHR_{ext} source, the estimation of OH_{exp} (using Eq. 3) under the OFR254 mode did not perform as well as that under the OFR185 mode (using Eq. 2). Firstly, we investigated the impacts of OHR_{ext}. Figure 4a1 showed the regression results of OH_{exp,est} and OH_{exp,dec} when OHR_{ext} ranged from 5 to 14 s⁻¹. The parameters x – z (FP_{IOHR,254}; IOHR: low external OHR) (Table S6) were obtained by fitting Eq. (3) to OH_{exp,dec}. In Fig. 4a2, the same set of fitted parameters FP_{IOHR,254} from Fig. 4a1 was used for a wider range of OHR_{ext} (5–21 s⁻¹). From the regression results (slopes of 1.050 and 1.024, R^2 of 0.890 and 0.894), the same set of parameters yielded similar estimation performance for OH_{exp} despite a wider range of OHR_{ext} in Fig. 4a2 compared to that of Fig. 4a1. At the same time, these results were not much different from those (slope = 1.071, $R^2 = 0.891$) using a refitted set of parameters (FP_{eOHR,254}; eOHR: extended external OHR) for the wider range of OHR_{ext} (Fig. 4a3). Even though the correlation was not as good as that in the OFR185 mode, approximately 85 % of the data points agreed within a factor of 2. We did not further extend the OHR_{ext} to values as high as those in the OFR185 mode as discussed above, since the OFR254 mode

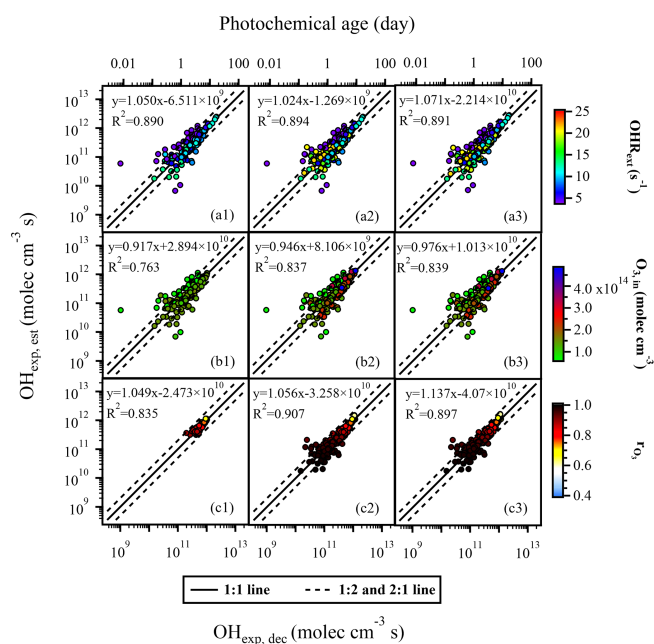


Figure 4. The regression results of $\text{OH}_{\text{exp,est}}$ and $\text{OH}_{\text{exp,dec}}$ when variations occurred in (a1–a3) OHR_{ext} , (b1–b3) input O_3 concentration, and (c1–c3) r_{O_3} . Compared to panels (a1), (b1), and (c1), panels (a2), (b2), and (c2) incorporated additional data points with extended OHR_{ext} , O_3 , in, and r_{O_3} values, respectively, but still utilized the fitting parameters $\text{FP}_{\text{IOHR},254}$, $\text{FP}_{\text{IO}_3,254}$, and $\text{FP}_{\text{mrO}_3,254}$ obtained from the lower or medium condition range to estimate $\text{OH}_{\text{exp,est}}$. In panels (a3), (b3), and (c3), all data points within the extended condition range were used to refit the parameters x – z , and the resulting $\text{FP}_{\text{eOHR},254}$, $\text{FP}_{\text{eO}_3,254}$, and $\text{FP}_{\text{erO}_3,254}$ were employed to estimate $\text{OH}_{\text{exp,est}}$.

was much less oxidative and might not be as suitable for simulating the oxidation chemistry of extremely high OHR_{ext} as that from direct emissions.

Similarly good correlations were observed when we only used the fitted parameters ($\text{FP}_{\text{IO}_3,254}$ and $\text{FP}_{\text{mrO}_3,254}$; IO_3 : low O_3 , in; mrO_3 : medium r_{O_3}) from narrow ranges of input O_3 concentration and r_{O_3} (Fig. 4b1 and c1, respectively) to reconstruct the $\text{OH}_{\text{exp,est}}$ values with extended ranges of these experimental conditions (Fig. 4b2 and c2, respectively). Such correlations were as good as those with refitted parameters ($\text{FP}_{\text{eO}_3,254}$ and $\text{FP}_{\text{erO}_3,254}$; eO_3 : extended O_3 , in; erO_3 : extended r_{O_3}) from data points in the extended ranges of O_3 concentration and r_{O_3} (Fig. 4b3 and c3, respectively). These observations thus indicate that, under the OFR254 mode, when OHR_{ext} , O_3 , in, and r_{O_3} vary within certain ranges (5 – 21 s^{-1} , 6.46×10^{13} – $4.8 \times 10^{14} \text{ molec. cm}^{-3}$, and 0.61 – 0.99 , respectively), Eq. (3) can be used to estimate OH radical levels reasonably well using the fitting parameters (x – z) obtained from a narrower range of data points.

Figure 5a and b depicted the correlation between $\text{OH}_{\text{exp,est}}$ estimated from Eq. (3) and $\text{OH}_{\text{exp,dec}}$ calculated from Eq. (1), with SO_2 and CO as OHR_{ext} sources, respectively.

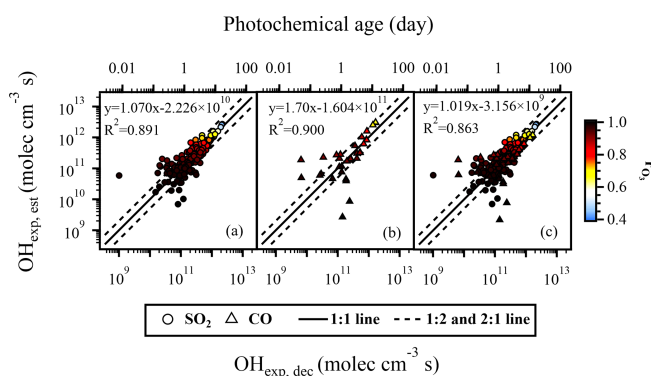


Figure 5. The regression results of $\text{OH}_{\text{exp,dec}}$ and $\text{OH}_{\text{exp,est}}$ in the OFR254 mode with (a) SO_2 and (b) CO as OHR_{ext} sources. (c) Results from all experiments (SO_2 and CO) in the OFR254 mode.

When using SO_2 as the OHR_{ext} source, approximately 86 % of the data points agreed within a factor of 2 (Fig. 5a). Similarly to the case of OFR185, when CO was used as the OHR_{ext} source, the data points were more scattered, with the percentage of data points within a factor of 2 dropping to only about 64 % (Fig. 5b). Figure 5c included data points using both SO_2 and CO as the OHR_{ext} sources. Overall, regardless of the OHR_{ext} source, when r_{O_3} was higher than 0.93, which meant a low UV intensity, the majority of data points for $\text{OH}_{\text{exp,est}}$ and $\text{OH}_{\text{exp,dec}}$ differed by a factor of 2 or more. It is therefore recommended that, when using the OFR254 mode, lamp power settings that are too low, for example, UV lamp voltage below 1.5 V, should be avoided in the case of our study.

4 Conclusions

A series of OH_{exp} estimation experiments using the PAM-OFR were conducted in the OFR185 and OFR254 modes to explore the applicability of the empirical equations under a wide range of conditions. The results indicate that, for the OFR185 mode, when varying the residence time, water vapor mixing ratio, and output O_3 concentration (as a surrogate for UV intensity) within certain ranges, the empirical equation (Eq. 2) for OH_{exp} proves to be effective in estimating OH_{exp} . Unless there is a significant change in OHR_{ext} , such as transitioning from ambient conditions to emission source conditions, there is no need to refit the parameters a – f in the estimation equation to estimate OH_{exp} . Compared with the OFR254 mode, the consistency between $\text{OH}_{\text{exp,est}}$ and $\text{OH}_{\text{exp,dec}}$ in the OFR185 mode is better. For the OFR254 mode, when OHR_{ext} , input O_3 concentration, and r_{O_3} vary within certain ranges, the empirical equation (Eq. 3) can be used to estimate OH_{exp} reasonably well using the parameters x – z obtained from a narrower range of data points. It is important to note that, for the OFR185 mode, the above conclusions are valid only if one already has a set of a – f

values that are appropriate for the specific UV lamps being used, as the $I_{185} : I_{254}$ that affects the OH_{exp} is lamp-specific. For a PAM-OFR that employs a different Hg lamp, a series of calibration experiments should be conducted in any case. Alternatively, based on the research by Rowe et al. (2020), the exponential relationship between the $a-f$ values and the $I_{185} : I_{254}$ could be used firstly to obtain a set of $a-f$ values suitable for the UV lamps being used.

To obtain reliable estimates of OH_{exp} using Eqs. (2) and (3) for the OFR185 mode and the OFR254 mode, respectively, it is desirable to have sufficient data points (that is, $\text{OH}_{\text{exp,dec}}$ from trace gas decay experiments) to fit the parameters for the calculation of $\text{OH}_{\text{exp,est}}$. There is currently no consensus on how many data points in trace gas decay experiments are enough for reliable fitted parameters, which could be important for in situ OH_{exp} estimation in field studies where a limited number of experiments are performed to reduce downtime. We aim to address this by random sampling from the data points in our experiments and determining the minimum number of experiments that are needed to obtain reliable OH_{exp} .

For the OFR185 mode, we firstly used randomly selected N data points from the 175 data points presented previously to fit the parameters ($a-f$) using Eq. (2). The fitted parameters were then used to reconstruct $\text{OH}_{\text{exp,est}}$ for all 175 data points. The $\text{OH}_{\text{exp,est}}$ values were then compared with the corresponding 175 $\text{OH}_{\text{exp,dec}}$ values. This procedure was repeated 10 times for each N , with N starting from 7 and reaching approximately 50 (Fig. 6a). The average R^2 , slope, and intercept from the 10 attempts were then shown as a function of N for experiments with SO_2 only (Fig. 6a) and for those with SO_2 and CO (Fig. 6b). It can be observed that around 30 data points are needed for experiments with SO_2 only, while around 20 data points are needed to have stable R^2 values and slopes when using both SO_2 and CO. For the OFR254 mode, the same procedure was applied to the 241 data points. It was not surprising that the results were a lot more scattered (Fig. 6c and d) compared to those for the OFR185 mode, given their performance shown in the previous section. Nevertheless, our analysis suggests that around 25 data points are needed to obtain reliable $\text{OH}_{\text{exp,est}}$ for the OFR254 mode, whether using SO_2 alone (Fig. 6c) or SO_2 and CO (Fig. 6d) for the trace gas decay experiments. Therefore, despite the limitation that this practice only randomly samples the data points without considering the range of any experimental conditions, our analysis suggests that 20–30 data points are normally needed to obtain reliable OH_{exp} for both the OFR185 and OFR254 modes.

Our study suggests that the $\text{OH}_{\text{exp,est}}$ estimated from the empirical equations agrees better with the $\text{OH}_{\text{exp,dec}}$ for the OFR185 mode (Fig. 3) than for the OFR254 mode (Fig. 5). This can be understood from the perspective of OH generation and its consumption by OHR_{ext} (Li et al., 2015). For the OFR185 mode, there are two pathways to generate OH radicals: the photolysis of H_2O and the photolysis of O_3 . For

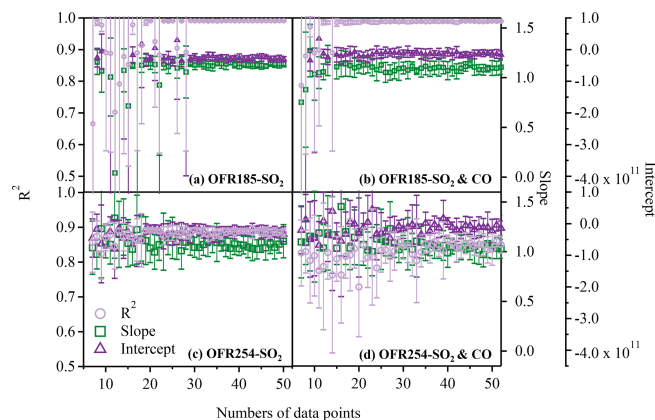


Figure 6. The regression results of $\text{OH}_{\text{exp,dec}}$ and $\text{OH}_{\text{exp,est}}$ (characterized by the R^2 , slope, and intercept) when different numbers of data points were chosen. (a) SO_2 as the OHR_{ext} source in the OFR185 mode, (b) SO_2 or CO as the OHR_{ext} source in the OFR185 mode, (c) SO_2 as the OHR_{ext} source in the OFR254 mode, and (d) SO_2 or CO as the OHR_{ext} source in the OFR254 mode.

the OFR254 mode, the main pathway for OH radical generation is solely the photolysis of O_3 . Consequently, when OHR_{ext} changes, the disruption to OH_{exp} in the system is more significant in the case of the OFR254 mode, while the OH_{exp} in the OFR185 mode remains more stable. In addition, pseudo-first-order kinetics between OH radicals and SO_2 or CO is assumed, with $[\text{OH}]$ being at a pseudo-steady state. However, the relatively low OH radical generation capacity in the OFR254 mode might not necessarily always fulfill such an assumption, leading to higher uncertainties for estimating OH_{exp} . Therefore, the OFR185 mode offers certain advantages, such as relatively high OH_{exp} , more accurate OH_{exp} estimation, and no external input of O_3 needed. However, for substances that exhibit strong absorption at the wavelength of 185 nm and are prone to photolysis, such as aromatic species (Peng et al., 2016), using the OFR254 mode is a better choice. For users of other OFRs (non-PAM-OFR) who would like to apply the conclusions above, at least two conditions must be met: (1) the concentration of $[\text{OH}]$ within the OFR should remain stable, and (2) the assumption of plug flow conditions should be acceptable, allowing the neglect of differences in the actual RTD, heterogeneity in the UV light intensity, and the concentration of radicals/oxidants at different points within the reactor, which are caused by different designs of reactors (such as wall materials, shapes, or volumes).

Data availability. The data shown in the paper are available on request from the corresponding authors (huangdd@saes.sh.cn and yongjieli@um.edu.mo).

Supplement. The supplement related to this article is available online at <https://doi.org/10.5194/amt-18-2509-2025-supplement>.

Author contributions. QL, DDH, and YJL conceived and planned the experiments. QL and YW carried out the experiments. QL, DDH, and YJL analyzed the data and took the lead in writing the paper. QL, DDH, YJL, ATL, and XC contributed to the interpretation of the results. SL, LZ, CYH, ST, QC, KIH, HW, KMM, and CH provided significant input during the revision of the paper. All authors provided feedback on the paper.

Competing interests. The contact author has declared that none of the authors has any competing interests.

Disclaimer. Publisher's note: Copernicus Publications remains neutral with regard to jurisdictional claims made in the text, published maps, institutional affiliations, or any other geographical representation in this paper. While Copernicus Publications makes every effort to include appropriate place names, the final responsibility lies with the authors.

Acknowledgements. Dan Dan Huang acknowledges the financial support from the National Key Research and Development Program of China (grant no. 2022YFC3703600), the Science and Technology Commission of Shanghai Municipality (grant no. 21230711000), and the General Fund of Natural Science Foundation of China (grant no. 42275124). Yong Jie Li acknowledges the financial support from the Science and Technology Development Fund, Macau SAR (grant nos. 0031/2023/AFJ and 0107/2023/RIA2), and multiyear research grants (grant nos. MYRG-GRG2023-00008-FST-UMDF and MYRG-GRG2024-00032-FST-UMDF) from the University of Macau.

Financial support. This research has been supported by the Fundo para o Desenvolvimento das Ciências e da Tecnologia (grant nos. 0031/2023/AFJ and 0107/2023/RIA2), the Universidade de Macau (grant nos. MYRG-GRG2023-00008-FST-UMDF and MYRG-GRG2024-00032-FST-UMDF), the National Key Research and Development Program of China (grant no. 2022YFC3703600), the Science and Technology Commission of Shanghai Municipality (grant no. 21230711000), and the National Natural Science Foundation of China (grant no. 42275124).

Review statement. This paper was edited by Meng Gao and reviewed by four anonymous referees.

References

- Atkinson, R. and Arey, J.: Atmospheric degradation of volatile organic compounds, *Chem. Rev.*, 103, 4605–4638, <https://doi.org/10.1021/cr0206420>, 2003.
- Atkinson, R., Baulch, D. L., Cox, R. A., Crowley, J. N., Hampson, R. F., Hynes, R. G., Jenkin, M. E., Rossi, M. J., Troe, J., and IUPAC Subcommittee: Evaluated kinetic and photochemical data for atmospheric chemistry: Volume II – gas phase reactions of organic species, *Atmos. Chem. Phys.*, 6, 3625–4055, <https://doi.org/10.5194/acp-6-3625-2006>, 2006.
- Barnet, P., Dommen, J., DeCarlo, P. F., Tritscher, T., Praplan, A. P., Platt, S. M., Prévôt, A. S. H., Donahue, N. M., and Baltensperger, U.: OH clock determination by proton transfer reaction mass spectrometry at an environmental chamber, *Atmos. Meas. Tech.*, 5, 647–656, <https://doi.org/10.5194/amt-5-647-2012>, 2012.
- Burkholder, J. B., Sander, S. P., Abbatt, J. P. D., Barker, J. R., Cappa, C., Crouse, J. D., Dibble, T. S., Huie, R. E., Kolb, C. E., Kurylo, M. J., Orkin, V. L., Percival, C. J., Wilmouth, D. M., and Wine, P. H.: Chemical kinetics and photochemical data for use in atmospheric studies, Evaluation Number 19, Jet Propulsion Laboratory, National Aeronautics and Space Administration, Pasadena, CA, <http://jpldataeval.jpl.nasa.gov> (last access: 7 December 2024), 2020.
- Cao, J., Wang, Q., Li, L., Zhang, Y., Tian, J., Chen, L. A., Ho, S. S. H., Wang, X., Chow, J. C., and Watson, J. G.: Evaluation of the oxidation flow reactor for particulate matter emission limit certification, *Atmos. Environ.*, 224, 117086, <https://doi.org/10.1016/j.atmosenv.2019.117086>, 2020.
- Cheng, X., Chen, Q., Jie Li, Y., Zheng, Y., Liao, K., and Huang, G.: Highly oxygenated organic molecules produced by the oxidation of benzene and toluene in a wide range of OH exposure and NO_x conditions, *Atmos. Chem. Phys.*, 21, 12005–12019, <https://doi.org/10.5194/acp-21-12005-2021>, 2021.
- Cheng, X., Li, Y. J., Zheng, Y., Liao, K., Koenig, T. K., Ge, Y., Zhu, T., Ye, C., Qiu, X., and Chen, Q.: Oxygenated organic molecules produced by low-NO_x photooxidation of aromatic compounds: contributions to secondary organic aerosol and steric hindrance, *Atmos. Chem. Phys.*, 24, 2099–2112, <https://doi.org/10.5194/acp-24-2099-2024>, 2024.
- Clerc, M. and Barat, F.: Kinetics of CO formation studied by far-UV flash photolysis of CO₂, *J. Chem. Phys.*, 46, 107–110, <https://doi.org/10.1063/1.1840358>, 1967.
- Cocker, D. R., Flagan, R. C., and Seinfeld, J. H.: State-of-the-art chamber facility for studying atmospheric aerosol chemistry, *Environ. Sci. Technol.*, 35, 2594–2601, <https://doi.org/10.1021/es0019169>, 2001.
- Cohen, N. and Heicklen, J.: The Oxidation of Inorganic Non-metallic Compounds, in: *Reactions of Non-Metallic Inorganic Compounds*, *Compr. Chem. Kinet.*, Elsevier, 1–137, [https://doi.org/10.1016/s0069-8040\(08\)70303-0](https://doi.org/10.1016/s0069-8040(08)70303-0), 1972.
- Ehhalt, D. H.: Photooxidation of trace gases in the troposphere Plenary Lecture, *Phys. Chem. Chem. Phys.*, 1, 5401–5408, <https://doi.org/10.1039/A905097C>, 1999.
- Friedman, B. and Farmer, D. K.: SOA and gas phase organic acid yields from the sequential photooxidation of seven monoterpenes, *Atmos. Environ.*, 187, 335–345, <https://doi.org/10.1016/j.atmosenv.2018.06.003>, 2018.
- Fuchs, H., Tan, Z., Lu, K., Bohn, B., Broch, S., Brown, S. S., Dong, H., Gomm, S., Häsel, R., He, L., Hofzumahaus, A., Hol-

- land, F., Li, X., Liu, Y., Lu, S., Min, K.-E., Rohrer, F., Shao, M., Wang, B., Wang, M., Wu, Y., Zeng, L., Zhang, Y., Wahner, A., and Zhang, Y.: OH reactivity at a rural site (Wangdu) in the North China Plain: contributions from OH reactants and experimental OH budget, *Atmos. Chem. Phys.*, 17, 645–661, <https://doi.org/10.5194/acp-17-645-2017>, 2017.
- George, I. J., Vlasenko, A., Slowik, J. G., Broekhuizen, K., and Abbatt, J. P. D.: Heterogeneous oxidation of saturated organic aerosols by hydroxyl radicals: uptake kinetics, condensed-phase products, and particle size change, *Atmos. Chem. Phys.*, 7, 4187–4201, <https://doi.org/10.5194/acp-7-4187-2007>, 2007.
- Hildebrandt, L., Donahue, N. M., and Pandis, S. N.: High formation of secondary organic aerosol from the photo-oxidation of toluene, *Atmos. Chem. Phys.*, 9, 2973–2986, <https://doi.org/10.5194/acp-9-2973-2009>, 2009.
- Kang, E., Root, M. J., Toohey, D. W., and Brune, W. H.: Introducing the concept of Potential Aerosol Mass (PAM), *Atmos. Chem. Phys.*, 7, 5727–5744, <https://doi.org/10.5194/acp-7-5727-2007>, 2007.
- Lambe, A. T., Ahern, A. T., Williams, L. R., Slowik, J. G., Wong, J. P. S., Abbatt, J. P. D., Brune, W. H., Ng, N. L., Wright, J. P., Croasdale, D. R., Worsnop, D. R., Davidovits, P., and Onasch, T. B.: Characterization of aerosol photooxidation flow reactors: heterogeneous oxidation, secondary organic aerosol formation and cloud condensation nuclei activity measurements, *Atmos. Meas. Tech.*, 4, 445–461, <https://doi.org/10.5194/amt-4-445-2011>, 2011.
- Li, R., Palm, B. B., Ortega, A. M., Hlywiak, J., Hu, W., Peng, Z., Day, D. A., Knote, C., Brune, W. H., and De Gouw, J. A.: Modeling the radical chemistry in an oxidation flow reactor: Radical formation and recycling, sensitivities, and the OH exposure estimation equation, *J. Phys. Chem. A*, 119, 4418–4432, <https://doi.org/10.1021/jp509534k>, 2015.
- Liao, K., Chen, Q., Liu, Y., Li, Y. J., Lambe, A. T., Zhu, T., Huang, R.-J., Zheng, Y., Cheng, X., and Miao, R.: Secondary organic aerosol formation of fleet vehicle emissions in China: Potential seasonality of spatial distributions, *Environ. Sci. Technol.*, 55, 7276–7286, <https://doi.org/10.1021/acs.est.0c08591>, 2021.
- Liu, J., Chu, B., Chen, T., Liu, C., Wang, L., Bao, X., and He, H.: Secondary organic aerosol formation from ambient air at an urban site in Beijing: effects of OH exposure and precursor concentrations, *Environ. Sci. Technol.*, 52, 6834–6841, <https://doi.org/10.1021/acs.est.7b05701>, 2018.
- Liu, T., Clegg, S. L., and Abbatt, J. P.: Fast oxidation of sulfur dioxide by hydrogen peroxide in deliquesced aerosol particles, *P. Natl. Acad. Sci. USA*, 117, 1354–1359, 2020.
- Lou, S., Holland, F., Rohrer, F., Lu, K., Bohn, B., Brauers, T., Chang, C. C., Fuchs, H., Häseler, R., Kita, K., Kondo, Y., Li, X., Shao, M., Zeng, L., Wahner, A., Zhang, Y., Wang, W., and Hofzumahaus, A.: Atmospheric OH reactivities in the Pearl River Delta – China in summer 2006: measurement and model results, *Atmos. Chem. Phys.*, 10, 11243–11260, <https://doi.org/10.5194/acp-10-11243-2010>, 2010.
- Lu, K., Zhang, Y., Su, H., Brauers, T., Chou, C. C., Hofzumahaus, A., Liu, S. C., Kita, K., Kondo, Y., and Shao, M.: Oxidant (O₃ + NO₂) production processes and formation regimes in Beijing, *J. Geophys. Res.-Atmos.*, 115, D07303, <https://doi.org/10.1029/2009JD012714>, 2010.
- Mao, J., Ren, X., Brune, W. H., Olson, J. R., Crawford, J. H., Fried, A., Huey, L. G., Cohen, R. C., Heikes, B., Singh, H. B., Blake, D. R., Sachse, G. W., Diskin, G. S., Hall, S. R., and Shetter, R. E.: Airborne measurement of OH reactivity during INTEX-B, *Atmos. Chem. Phys.*, 9, 163–173, <https://doi.org/10.5194/acp-9-163-2009>, 2009.
- Nakashima, Y., Kamei, N., Kobayashi, S., and Kajii, Y.: Total OH reactivity and VOC analyses for gasoline vehicular exhaust with a chassis dynamometer, *Atmos. Environ.*, 44, 468–475, <https://doi.org/10.1016/j.atmosenv.2009.11.006>, 2010.
- Ono, R., Nakagawa, Y., Tokumitsu, Y., Matsumoto, H., and Oda, T.: Effect of humidity on the production of ozone and other radicals by low-pressure mercury lamps, *J. Photochem. Photobiol. A*, 274, 13–19, <https://doi.org/10.1016/j.jphotochem.2013.09.012>, 2014.
- Palm, B. B., de Sá, S. S., Day, D. A., Campuzano-Jost, P., Hu, W., Seco, R., Sjostedt, S. J., Park, J.-H., Guenther, A. B., Kim, S., Brito, J., Wurm, F., Artaxo, P., Thalman, R., Wang, J., Yee, L. D., Wernis, R., Isaacman-VanWertz, G., Goldstein, A. H., Liu, Y., Springston, S. R., Souza, R., Newburn, M. K., Alexander, M. L., Martin, S. T., and Jimenez, J. L.: Secondary organic aerosol formation from ambient air in an oxidation flow reactor in central Amazonia, *Atmos. Chem. Phys.*, 18, 467–493, <https://doi.org/10.5194/acp-18-467-2018>, 2018.
- Pan, T., Lambe, A. T., Hu, W., He, Y., Hu, M., Zhou, H., Wang, X., Hu, Q., Chen, H., Zhao, Y., Huang, Y., Worsnop, D. R., Peng, Z., Morris, M. A., Day, D. A., Campuzano-Jost, P., Jimenez, J.-L., and Jathar, S. H.: A comprehensive evaluation of enhanced temperature influence on gas and aerosol chemistry in the lamp-enclosed oxidation flow reactor (OFR) system, *Atmos. Meas. Tech.*, 17, 4915–4939, <https://doi.org/10.5194/amt-17-4915-2024>, 2024.
- Peng, Z. and Jimenez, J. L.: KinSim: a research-grade, user-friendly, visual kinetics simulator for chemical-kinetics and environmental-chemistry teaching, *J. Chem. Educ.*, 96, 806–811, <https://doi.org/10.1021/acs.jchemed.9b00033>, 2019.
- Peng, Z. and Jimenez, J. L.: Radical chemistry in oxidation flow reactors for atmospheric chemistry research, *Chem. Soc. Rev.*, 49, 2570–2616, <https://doi.org/10.1039/C9CS00766K>, 2020.
- Peng, Z., Day, D. A., Stark, H., Li, R., Lee-Taylor, J., Palm, B. B., Brune, W. H., and Jimenez, J. L.: HO_x radical chemistry in oxidation flow reactors with low-pressure mercury lamps systematically examined by modeling, *Atmos. Meas. Tech.*, 8, 4863–4890, <https://doi.org/10.5194/amt-8-4863-2015>, 2015.
- Peng, Z., Day, D. A., Ortega, A. M., Palm, B. B., Hu, W., Stark, H., Li, R., Tsigaridis, K., Brune, W. H., and Jimenez, J. L.: Non-OH chemistry in oxidation flow reactors for the study of atmospheric chemistry systematically examined by modeling, *Atmos. Chem. Phys.*, 16, 4283–4305, <https://doi.org/10.5194/acp-16-4283-2016>, 2016.
- Rowe, J. P., Lambe, A. T., and Brune, W. H.: Technical Note: Effect of varying the $\lambda = 185$ and 254 nm photon flux ratio on radical generation in oxidation flow reactors, *Atmos. Chem. Phys.*, 20, 13417–13424, <https://doi.org/10.5194/acp-20-13417-2020>, 2020.
- Seinfeld, J. H. and Pandis, S. N.: Atmospheric chemistry and physics: from air pollution to climate change, John Wiley & Sons, Inc., ISBN 9781119221166, 2016.

- Stone, D., Whalley, L. K., and Heard, D. E.: Tropospheric OH and HO₂ radicals: field measurements and model comparisons, *Chem. Soc. Rev.*, 41, 6348–6404, <https://doi.org/10.1039/C2CS35140D>, 2012.
- Tan, Z., Fuchs, H., Lu, K., Hofzumahaus, A., Bohn, B., Broch, S., Dong, H., Gomm, S., Häseler, R., He, L., Holland, F., Li, X., Liu, Y., Lu, S., Rohrer, F., Shao, M., Wang, B., Wang, M., Wu, Y., Zeng, L., Zhang, Y., Wahner, A., and Zhang, Y.: Radical chemistry at a rural site (Wangdu) in the North China Plain: observation and model calculations of OH, HO₂ and RO₂ radicals, *Atmos. Chem. Phys.*, 17, 663–690, <https://doi.org/10.5194/acp-17-663-2017>, 2017.
- Tan, Z., Rohrer, F., Lu, K., Ma, X., Bohn, B., Broch, S., Dong, H., Fuchs, H., Gkatzelis, G. I., Hofzumahaus, A., Holland, F., Li, X., Liu, Y., Liu, Y., Novelli, A., Shao, M., Wang, H., Wu, Y., Zeng, L., Hu, M., Kiendler-Scharr, A., Wahner, A., and Zhang, Y.: Wintertime photochemistry in Beijing: observations of RO_x radical concentrations in the North China Plain during the BEST-ONE campaign, *Atmos. Chem. Phys.*, 18, 12391–12411, <https://doi.org/10.5194/acp-18-12391-2018>, 2018.
- Wang, N., Zannoni, N., Ernle, L., Bekö, G., Wargocki, P., Li, M., Weschler, C. J., and Williams, J.: Total OH reactivity of emissions from humans: in situ measurement and budget analysis, *Environ. Sci. Technol.*, 55, 149–159, <https://doi.org/10.1021/acs.est.0c04206>, 2020.
- Wang, X., Liu, T., Bernard, F., Ding, X., Wen, S., Zhang, Y., Zhang, Z., He, Q., Lü, S., Chen, J., Saunders, S., and Yu, J.: Design and characterization of a smog chamber for studying gas-phase chemical mechanisms and aerosol formation, *Atmos. Meas. Tech.*, 7, 301–313, <https://doi.org/10.5194/amt-7-301-2014>, 2014.
- Yang, Y., Shao, M., Keßel, S., Li, Y., Lu, K., Lu, S., Williams, J., Zhang, Y., Zeng, L., Nölscher, A. C., Wu, Y., Wang, X., and Zheng, J.: How the OH reactivity affects the ozone production efficiency: case studies in Beijing and Heshan, China, *Atmos. Chem. Phys.*, 17, 7127–7142, <https://doi.org/10.5194/acp-17-7127-2017>, 2017.
- You, X., Wang, H., Goos, E., Sung, C.-J., and Klippenstein, S. J.: Reaction kinetics of CO + HO₂ → products: ab initio transition state theory study with master equation modeling, *J. Phys. Chem. A*, 111, 4031–4042, <https://doi.org/10.1021/jp067597a>, 2007.
- Zhang, Z., Xu, W., Lambe, A. T., Hu, W., Liu, T., and Sun, Y.: Insights Into Formation and Aging of Secondary Organic Aerosol From Oxidation Flow Reactors: A Review, *Curr. Pollut. Rep.*, 10, 1–14, <https://doi.org/10.1007/s40726-024-00309-7>, 2024.